JOURNAL OF PROPULSION AND POWER
Vol. 14, No. 2, March–April 1998

Investigation of Cryogenic Propellant Flames Using Computerized Tomography of Emission Images

Gerald Herding,* Ray Snyder,* Carlos Rolon,† and Sébastien Candel‡
Centre National de la Recherche Scientifique, Châtenay-Malabry F-92295, France

Cryogenic propellant combustion is investigated in this paper. It is shown that the mean flame structure may be obtained by applying computerized tomography principles to oxygen–hydrogen (OH) emission images obtained from experiments on a shear coaxial injector. The data correspond to injection conditions typical of those found in rocket motors, but to lower operating pressures of 1, 5, and 10 bar. The transformed emission images yield the mean volumetric OH emission distribution. This quantity may be roughly interpreted as the mean volumetric rate of reaction. The data provide the location of the mean flame zone and confirm that stabilization takes place in the immediate vicinity of the injection plane.

I. Introduction

LIQUID oxygen–gaseous hydrogen rocket engines have been used for a number of years because they yield the high specific-impulse values needed in space propulsion applications. Cryogenic propellants thus diminish the cost per mass of payload in orbit, but pose specific storage, handling, and operating problems. Current rocket motor design relies on extensive experience and technological expertise. The detailed processes involved in cyrogenic combustion are, however, not yet fully documented. An improved understanding of the mode of flame stabilization and of the flame structure in the near field of the injector head would be quite valuable. This information could be used to improve design methodologies and enhance reliability of operation. Such information would be useful for more accurate predictions of heat transfer rates to the engine walls. In this context, knowledge about whether the flame is stabilized right on the injector lip or at a distance as a lifted flame is of considerable interest.

The stabilization region is specifically investigated in this paper on the basis of experiments carried out on a cryogenic model scale combustor designated as Mascotte. This facility, operated by ONERA, is dedicated to basic research and technological studies. Data gathered at this facility include planar laser-induced fluorescence (LIF), planar laser light scattering, and emission imaging. Simultaneous recording of light elastic scattering and hydroxyl radical (OH) fluorescence images has allowed identification of the flame stabilization. When the liquid oxygen (LOX) is injected by a central tube and is surrounded by an annulus of high-speed gaseous hydrogen, it is shown[1] that the flame is established in the outer boundary of the LOX jet, where the hydrogen stream velocity is low. It is also found that the laser-induced OH–fluorescence signal level remains in the same range over the zone visualized, with little change in the signal amplitude as a function of the axial distance. However, the emission images of the excited OH radical appear to yield a different picture of the flame stabilization region. The emission amplitude is low close to the injector and increases rapidly at a distance. From these specific features one may be led to conclude that a pilot flame exists in the inner boundary of the oxygen tube, as proposed by Mayer and Tamura[2] from their observations at a different cryogenic facility. This pilot flame would then be followed by an intermediate region of weak reaction rate and a rapid increase of combustion at a distance from the injector.

It is shown in this paper that new insight into this problem may be obtained by applying computerized tomography principles to the time-averaged emission images. Using an Abel transformation, one obtains radial profiles of volumetric light emission from the axisymmetric line-of-sight (LOS) images. This technique was previously applied to radiant emissions from flames[3] and to emission images of cryogenic combustion.[4] The deconvolution method[4] forms the basis of our own method of computerized tomography. Using this processing tool, we examine the structure of typical cryogenic flames. The computer-transformed images reveal that the mean volumetric light emission stays in the same range over the whole visualization zone. This result is consistent with the fluorescence images, confirming that the flame begins in the immediate vicinity of the injector. In this investigation, the raw data are constituted by the light radiated by OH radicals. This light originates from thermally excited OH molecules in equilibrium, or by chemically excited OH*. It is generally admitted that thermal emission from OH at typical flame temperatures is negligible compared with chemiluminescent emissions.[3] One may then interpret emission from OH radicals as a signature of the reaction zone. Thus, the mean volumetric OH* emission may be interpreted roughly in terms of the mean heat release in the flame. The numerically transformed images may then be used to determine the mean flame position and its axial evolution. The influence of operating conditions defined by dimensionless groups may be investigated on this basis. The data indicate that flame shapes in the injector near field are governed by atomization. This has been shown by Snyder et al.[5] and the processed images confirm the previous results. To begin with, Sec. II reviews the Abel transformation method and its underlying assumptions. Specific details of the present application are also described in Sec. II. A short description of the experimental setup and of the operational parameters is given in Sec. III. Results are discussed and interpreted in Sec. IV.

II. Abel Transformation Method

It is assumed in what follows that the mean flowfield being analyzed is axisymmetric. Let us consider the light emitted by a given region of interest and recorded by a detector in the (x, y) plane (Fig. 1). When self-absorption and scattering of

---

Received Jan. 27, 1997; revision received July 25, 1997; accepted for publication Aug. 10, 1997.

*EM2C Laboratory, Ecole Centrale Paris.

†Professor, EM2C Laboratory, Ecole Centrale Paris.

‡Professor, EM2C Laboratory, Ecole Centrale Paris. Member AIAA.

the emitted light may be neglected, the signal $S_p(x, y)$ detected by the pixel (x, y) of the charge-coupled device (CCD) camera is a sum over the LOS of the local intensity, and one may write

$$S_p(x, y) = \eta_{\text{opt}} \int_0^Z i(x, y, z)\, \mathrm{d}z \qquad (1)$$

where z is the distance from the CCD camera, Z designates the maximum distance from which light may be radiated, and $i(x, y, z)$ is the volumetric light emission intensity. The constant η_{opt} describes the solid angle of collection and the transmission efficiency of optical components. In the present experiments, η_{opt} is constant over the range of frequencies $\Delta\nu$ of interest. Assuming that the mean $i(x, y, z)$ has a rotational symmetry with respect to the injector axis, and that this axis is perpendicular to the LOS of the camera, then by changing the variable of integration into $r = (y^2 + z^2)^{1/2}$, one obtains

$$S_p(x, y) = \eta_{\text{opt}} \int_y^R i(x, r) \frac{2r}{(r^2 - y^2)^{1/2}}\, \mathrm{d}r \qquad (2)$$

where r is the radial distance from the symmetry axis, and R designates the maximum distance at which light may be emitted. Equation (2) is an Abel's integral, which may be inverted to get $i(x, r)^{6-8}$:

$$i(x, r) = \frac{1}{\eta_{\text{opt}}} \frac{(-1)}{\pi} \int_r^R \frac{\partial S_p(x, y)}{\partial y} \frac{\mathrm{d}y}{(y^2 - r^2)^{1/2}} \qquad (3)$$

This expression indicates that the local volumetric intensity may be calculated as an integral of the derivative of the detected signal $\partial S_p/\partial y$, weighted by a kernel $(y^2 - r^2)^{-1/2}$. Because it involves the derivative $(\partial S_p/\partial y)$ of the detected signal, the inversion method is sensitive to noise. This sensitivity increases toward the center because of the decreased volume contributing to the signal. To see this more clearly, let us consider the vicinity of $y = r$ and write $y = r + \eta$. One then finds that for small values of η, $\mathrm{d}y/(r^2 - y^2)^{1/2} \simeq \mathrm{d}\eta/(2r\eta)^{1/2}$, which indicates that noise in the data is amplified when r becomes small. The effect of noise on reconstruction accuracy is examined in further detail by Hughey and Santavicca.[7]

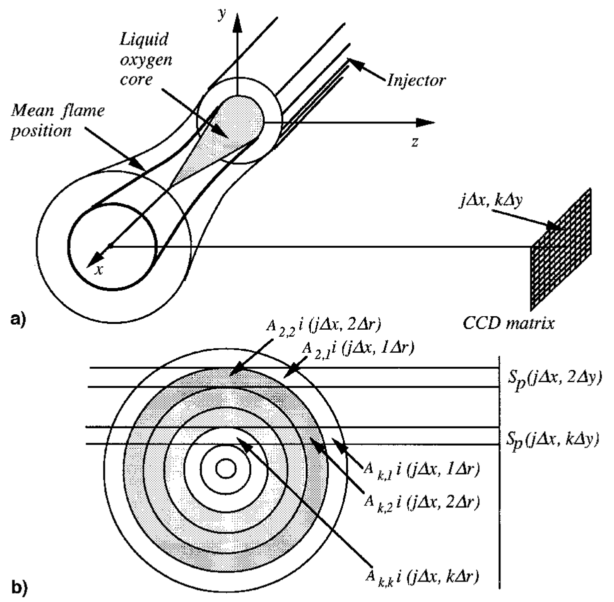

Fig. 1 a) Schematic view of LOS OH*-emission detection. b) Principle of algebraic reconstruction used to invert $S_p(x, y)$. Inversion of A allows calculation of $i(x, r)$.

Although Eq. (3) is well suited to theoretical studies of the problem, practical inversion of the signal detected by the camera is best accomplished with a discrete version of Eq. (2). One may write the signal $S_p(j\Delta x, k\Delta y)$, detected by the (j, k) pixel as a discrete sum:

$$S_p(j\Delta x, k\Delta y) = \sum_{l=1}^{k} A_{kl}\, i(j\Delta x, l\Delta r) \qquad (4)$$

where $\Delta x = \Delta y$ designates the pixel size and $A_{kl}\Delta x$ represents the volume in which $i(j\Delta x, l\Delta r)$ occurs and contributes to $S_p(j\Delta x, k\Delta y)$. The inverse of the matrix A multiplied by the signal vector $\boldsymbol{S}_p$ in each section x yields the matrix of $i(x, r)$. This form of algebraic reconstruction technique, more commonly known as onion peeling, is known to yield good results if some filtering or data smoothing is carried out before inversion.[7]

Spatial filtering is applicable when physical spatial frequencies are distinct from those of the noise. In the present case, the intensified CCD camera noise is essentially random and there is no spatial correlation between neighboring pixels. Consequently, the typical spatial frequency of this random noise is the inverse of two pixel sizes $(2\Delta y)^{-1}$. There are no other distinguishable frequencies characterizing other sources of noise, such as inhomogeneities of light transmission of the optical components (windows, filters, etc.). It follows that a low-pass filter may be used to smooth the data. In the whole area, median filtering effectively removes random noise from the raw image while preserving edges. Near the axis, data smoothing is important, and is obtained by an additional spatial averaging. To account for the differences in sensitivity of the CCD matrix, one has to divide the image by an image of reference (flat fielding). This reference represents the relative sensitivity of the pixels, and is obtained by mapping an object that is illuminated in a homogeneous manner by a light source at the wavelength of interest.

III. Experimental Setup

The Mascotte facility[9] is shown schematically in Fig. 2. The combustor comprises a single coaxial injector fed with liquid oxygen and gaseous hydrogen. In the present version and in our experiments, the maximum chamber pressure $p_g = 10$ bar, LOX is subcooled to $T_{\text{LOX}} = 77$ K, and the gaseous hydrogen is injected at room temperature. In a later version, supercritical conditions will be available to approach real conditions prevailing in rocket engines under steady-state operation. The combustion chamber is a square duct with a cross section of 50×50 mm^2, and the visualized area of 50×75 mm^2 begins at the injector. Injection conditions at 1, 5, and 10 bar are collected in Table 1.

Table 1 shows the LOX injection velocity v_l, the Weber number We_l, momentum flux ratio J, and mixture ratio E. The gaseous Weber number $We_g = (\rho_g v_g^2 d_l)/\sigma_l$ is based on the initial jet diameter $d_l = 5$ mm. The dimensionless numbers We_l and J gathered in Table 1 have been selected because they essentially control the liquid jet disintegration and atomization and, therefore, influence the flame structure. Cold flow experiments[10] indicate that $J = \rho_g v_g^2/\rho_l v_l^2$ controls the jet disintegration. It is indicated that an acceptable atomization is obtained when J exceeds a critical value

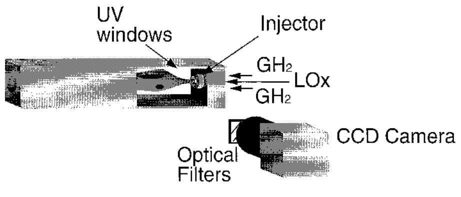

Fig. 2 Experimental setup showing the cryogenic combustion chamber with a single injector element. Two lateral quartz windows allow optical access. A CCD camera placed at right angles to the axis records the OH* emission signal.

of 10. It was then decided to vary the J number around this critical value. More information on the operating conditions and the governing parameters is given in Ref. 5.

Emission of OH* radicals is detected in the present experiments to locate regions of intense combustion. Radiation from OH* takes place in the near uv range between 306 and 320 nm, and this band of wavelengths is clearly separated from those of oxygen and water. In the experiments carried out at atmospheric pressure, light detection was achieved with a Photometrics slow-scan CCD camera, featuring 576 × 378 pixels with 16 bits depth. The other experiments were carried out with a Princeton Instruments CCD camera (578 × 384 pixels with 12 bits depth). The pixels were grouped 2 × 2 to compress the data and increase the imaging rate. Images were stored at a rate of 0.4 and 10 Hz with the Photometrics and Princeton cameras, respectively. Both systems were equipped with a Nikon-105 mm $f = 4.5$ uv objective. A UG-5 Schott glass filter was used to block radiation above 400 nm, and two WG 305 filters were employed to suppress radiation below 283 nm while passing 55–80% of the light emitted between 306 and 320 nm where chemiluminescence is observed. The camera was placed on one side of the combustor at right angles with respect to the axis. The field of view was 42 × 63 mm^2 at 1 bar and 50 × 75 mm^2 at 5 and 10 bar. At 1 bar, the emission signal was weaker than at higher pressures, and the exposure time was set equal to 50 μs. Exposure times of 10–20 μs were used at 5 and 10 bar. The solid angle for light collection was $\Omega = 4 \times 10^{-3}$ sr, corresponding to a viewing half-angle $\varepsilon = 1.9$ deg. In this situation, the light rays in the flame region are nearly parallel and the Abel transformation may be used without correction.

IV. Results and Discussion

It is first useful to examine the successive steps of the processing method. These are shown in Fig. 3. The ensemble-average emission images constitute the raw data. The averaging

Table 1 Operating conditions for experiments performed at the Mascotte facility

Point of operation	v_l, m/s	We_g $(\rho_g v_g^2 d_l)/\sigma_l \times 10^{-3}$	J $(\rho_g v_g^2)/(\rho_l v_l^2)$	E $(\dot m_l/\dot m_g)$, bar 1	5	10
A	2.2	27	14	3.3	3.0	2.1
C	2.2	13	6.5	5.0	4.5	3.2
D'	1.8	13	10	4.0	3.6	2.5

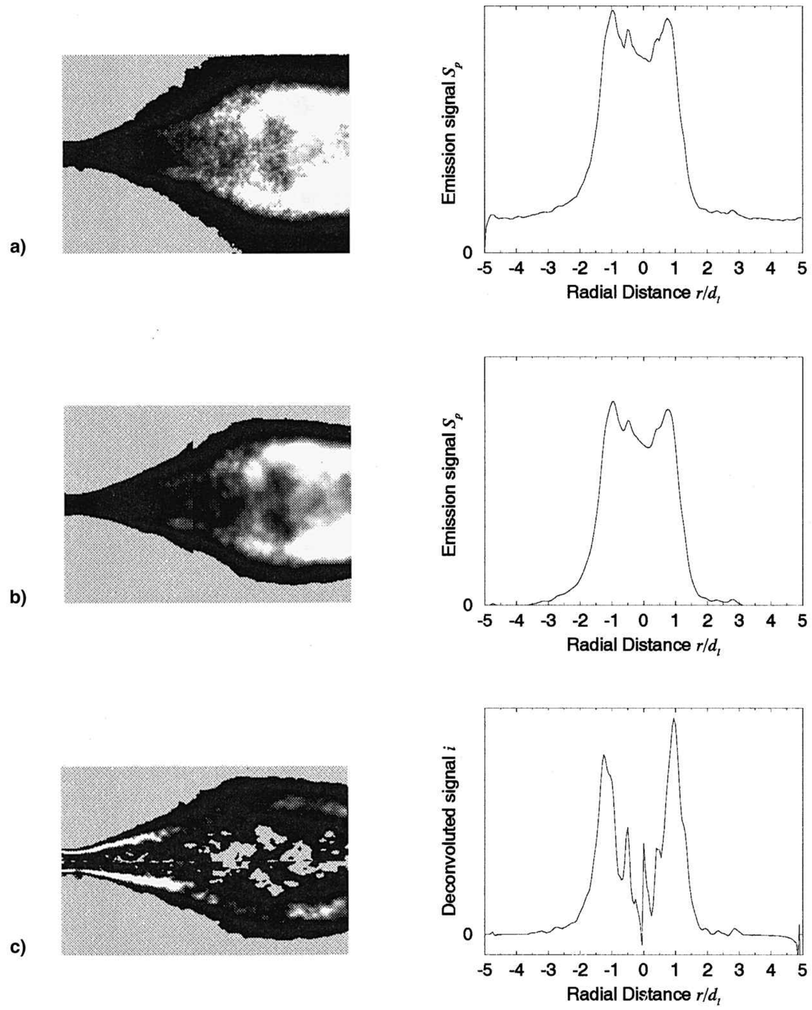

Fig. 3 Three light emission images (left), and radial emission profiles at an axial distance $x = 4d_l$ (right); operating condition A, $p = 5$ bar: a) OH*-light emission image; b) treated emission image, subtraction of diffusive light and low pass filtering; and c) deconvolved image using Abel's transformation.

is carried out over a set of images recorded during a single run of the cryogenic combustion facility (20 and 140 images at atmospheric pressure and elevated pressure experiments, respectively). The average images are quite symmetric, a necessary condition for the validity of the method, and their typical appearance is illustrated at the top of Fig. 3. As shown in Fig. 3, the transverse profile plotted in a section located at a distance $x = 4d_l$ does not fall to 0 when leaving the region where OH* emission occurs, but stays at a nearly constant level. This background level, which corresponds to scattered light, has to be subtracted from the radial profiles before deconvolution. The level of this scattered light increases slightly with axial distance; to take this into account, two different zones were defined in which a constant value was subtracted from the images. To smooth the data, a median filter of variable window size was used. The window size for this filter is increased with axial distance as the spatial frequencies decrease with distance from the injector and allow stronger filtering. At the injector, the filter window size is smallest (3 × 3 pixels, where 1 pixel corresponds to 0.25 mm) because in this region one expects sharp physical gradients in the data. This filtering has, however, no influence on the accuracy of the method because the ratio of the gradients as a result of noise to the physical gradients is the error-determining parameter. Near the axis, the data are filtered by taking the average of (5 × 5) ensembles of pixels to obtain the smoothest data, where the procedure is most sensitive to noise. A deconvolved image is also shown in Fig. 3. This image indicates the sensitivity of the method to noise near the axis, where the deconvolved signal may become negative or feature local peaks. In the original emission image, the signal detected by the camera $S_p(x, y)$ is faint close to the injector and increases rapidly at a distance, suggesting a flame stabilization involving a pilot flame. The deconvolved image is notably different, featuring high volumetric intensity values close to the injector. The volumetric intensity keeps the same order of magnitude and then decreases slightly with increasing axial distance.

The deconvolved image is not perfectly symmetric because numerical inversion is applied independently to the upper and lower part of the emission data. The difference between the

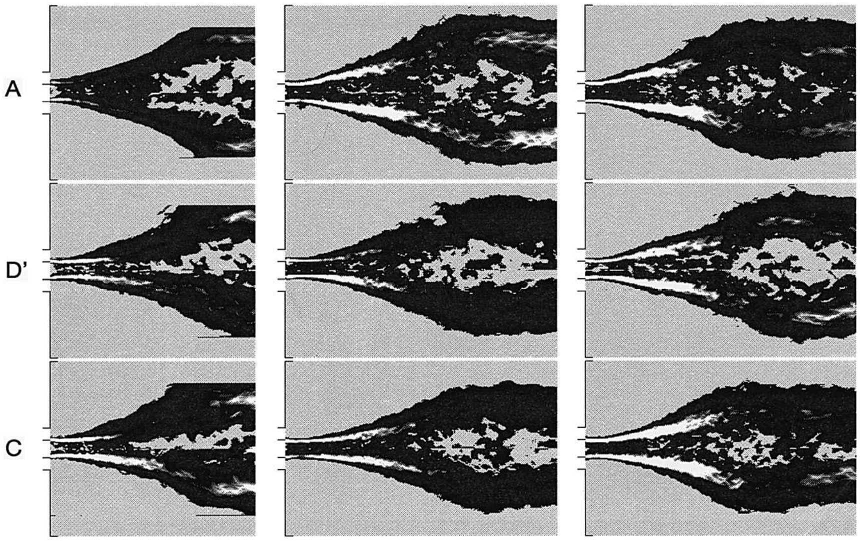

Fig. 4 Deconvolved emission images using Abel's transformation. The images were obtained at ONERA's Mascotte facility. Each row represents the operating conditions referred to in the text as A, D', and C at 1, 5, and 10 bar, respectively (from left to right).

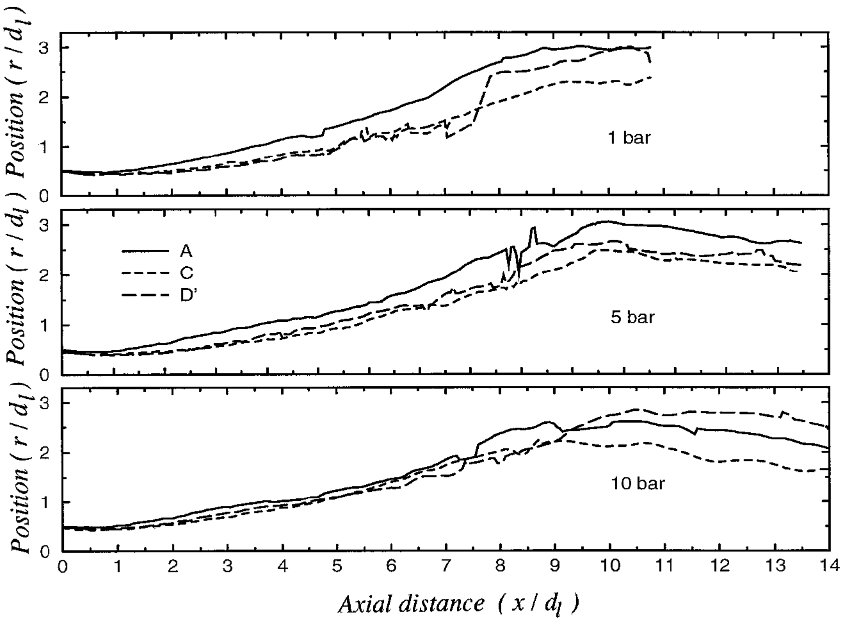

Fig. 5 Position of maximum time-averaged $i(x, r)$. Three different operating points (A, C, and D') are each compared at 1, 5, and 10 bar, respectively. At 1 bar, the visualized zone is shorter.

upper and lower distributions of volumetric light intensity gives an estimate of the influence of measurement imperfections and noise.

Fig. 4 displays deconvolved emission images deduced from the ensemble-average emission data corresponding to the operating conditions given in Table 1. For the data at 1 bar, the visualization area is somewhat smaller than that corresponding to the 5- and 10-bar experiments. The distribution of OH*-light intensity indicates that the mean reaction region begins at the LOX tube lip. The region of light emission is initially thin and nearly cylindrical. This region expands further downstream into a thick shell surrounding the gaseous oxygen and LOX droplet spray formed after jet breakup. The volumetric OH* emission intensity is then spread over a region of finite thickness. After an initial expansion, the mean flame becomes annular. The inner and outer diameters of the flame volume slowly decrease with axial distance as the oxygen convected in the central region is being consumed. The rate of expansion of the initial mean flame is greatest when the injector operates under condition A, corresponding to the largest value of J. The flame develops more rapidly and the reactive volume is broader in this case. This behavior is less pronounced as pressure is increased. These observations are in agreement with those made in Ref. 5.

To be more quantitative, it is worth trying to determine the mean flame position. For this, one may consider the radial profiles of the deconvolved signal and locate the position of the maximum light emission, which will be taken as the flame location. The signal level is smallest near the centerline (the fluctuating behavior of the signal in this region is merely a result of increased sensitivity to noise). The deconvolved signal then reaches a maximum level at a certain radial position, and decreases afterward to nearly 0 close to the chamber walls.

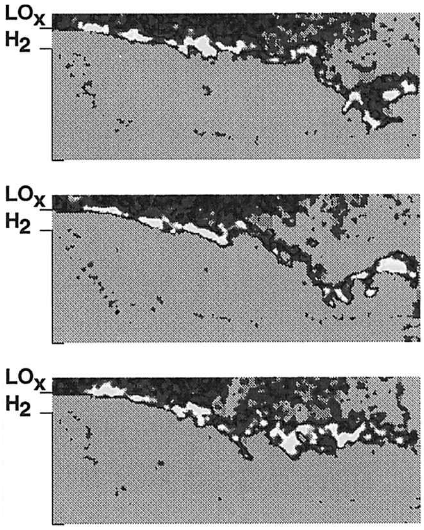

Fig. 6 Typical OH–LIF images. Laser pumping wavelength λ = 283.92 nm, pulse duration = 20 ns, and pulse energy = 25 mJ. Operating condition A, p = 5 bar.

In an ideal situation, the signal should be somewhat higher near the centerline because of the presence of the LOX spray, which scatters some of the light emitted in the back of the flame. However, this does not affect the deconvolution in the outer reaction region, where the signal is highest and no spray is present. As a consequence, the radial profiles deduced from the transformation procedure are accurate in the region where maximum volumetric light emission is located. The position of time-averaged maximum volumetric light emission intensity may be obtained with the following procedure. A Gaussian fit is calculated in each axial section of the deconvolved image, then the position of the maximum of this fit is determined; the axial variation of this quantity is displayed in Fig. 5. The flame corresponding to operating condition A develops most rapidly. The maximum positions corresponding to operating points C and D′ are quite close in the beginning, but at a certain distance the flame expands more rapidly when the combustor operates under condition D′ (intermediate momentum ratio).

At this point, it is worth examining OH-laser-induced fluorescence data recorded in another series of experiments at the cryogenic combustion facility.[5] Figure 6 displays a typical set of images. The laser sheet illuminates the reaction zone from below, so that the photograph shows only the lower half of the combustor. The OH radical is found on a thin, highly corrugated layer starting at the injector lip. The maximum level of OH remains in the same range, and the reactive layer lies initially along the jet of LOX, its position rather constant. Further downstream, as the LOX jet breaks down, the reactive layer becomes strongly wrinkled and moves by large amounts from one frame to the next. These observations are consistent with the mean flame distributions deduced by numerical tomography. We will see that the mean flame location deduced from OH–LIF data agrees with that found from numerical tomography of emission data.

Figure 7 compares experimental flame locations deduced from OH*-emission and OH–fluorescence images at the operating point C. Mean flame positions were obtained from the fluorescence images (as explained in more detail in Ref. 5) and from the deconvolved emission images by fitting the volumetric light distribution and searching the maximum in each axial section. Figure 7 also shows the mean half-emission width, obtained by calculating the contour for all instantaneous images. To this purpose, a locally variable axial threshold of 30% of the maximum emission in that column was used to obtain the contour points at each axial distance.

The consistency between the mean position of the flame and the maximum volumetric light emission intensity is quite remarkable. It could have been different if the volumetric light emission were to depend on the radial position where it occurs. This result is interesting because it indicates that the mean flame position may be determined by processing emission images, rather than from LIF images. This greatly simplifies experimentation, because fluorescence images require a pumping laser and additional windows for laser light transmission. Figure 7 also indicates that the half-width of the emission images is far greater than the mean flame distance with respect to the axis. This is partly because of the turbulence producing flame wrinkling, which in turn causes emission to occur from a vol-

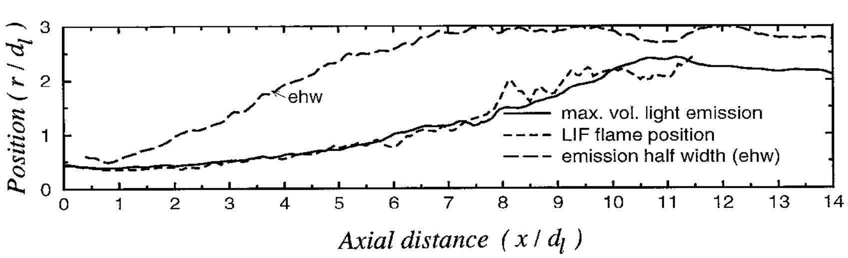

Fig. 7 Comparison of mean half-size of flame distribution, flame position from LIF images,[5] and position where maximum volumetric light emission occurs.

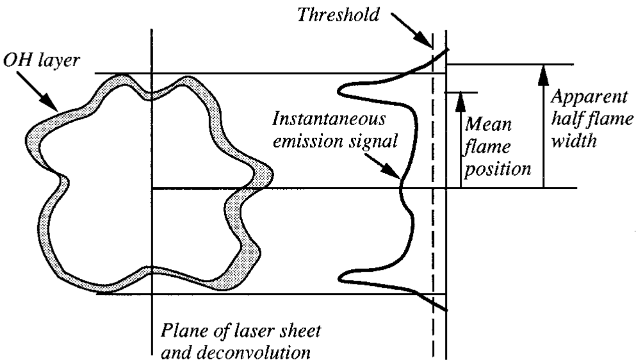

Fig. 8 Left, a cut across the flame in one section located at an axial distance x. Right, the emission signal detected by one column of the CCD camera. This figure indicates that the apparent flame half-width always exceeds the value found for the flame position.

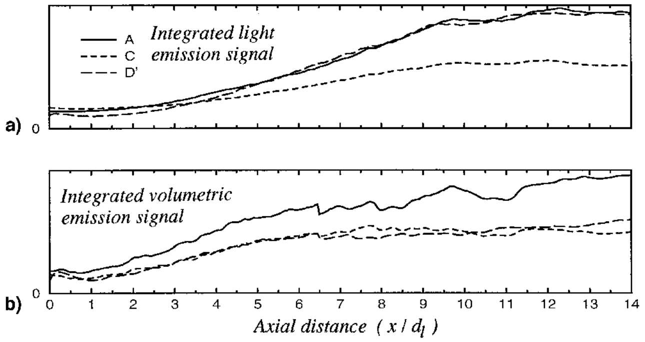

Fig. 9 Axial evolution of the signal integrated over each section (over each column of the CCD camera): a) OH* light emission; and b) volumetric light emission obtained from computerized deconvolution of emission images.

ume that envelops the mean flame volume. These phenomena are explained schematically in Fig. 8.

It was noticed that the signal level in the deconvolved images does not increase with axial distance, as in the raw emission images, but stays at the same level or even decreases slightly. It is also interesting to examine the axial evolution of the signal integrated over each transverse section, as plotted in Fig. 9. Surprisingly, this integrated signal shows approximately the same behavior for the raw emission images and for the deconvolved images. The same trend is also observable in the fluorescence images.[5] Although there are no general variations in the fluorescence images, the flame gets thicker downstream, and this causes a rise in the integrated values.

V. Conclusions

Computerized tomography is used to deconvolve mean emission images of OH radicals. The method is applied to cryogenic flames and produces acceptable data in this difficult situation. Results indicate that the flame intensity remains essentially constant over the region investigated, but that flame wrinkling is responsible for the production of flame fronts, causing an augmentation of the integrated emission intensity and reaction rate as the axial distance increases. It is suggested that the mean flame position may be deduced from the emission images when the data are rotationally symmetric in the mean. The results confirm that the flame is stabilized in the immediate vicinity of the injector. This result, deduced from a different set of diagnostic techniques, is well confirmed by the deconvolved images obtained in this paper. In contrast, a pilot-flame mode of stabilization with an initially weak reaction intensity, which might be imagined from a direct examination of the raw emission images, does not conform with the present data.

Acknowledgments

This study was supported in part by the Société Européenne de Propulsion and the Centre National d'Etudes Spatiales (CNES). Gerald Herding is supported by CNES and DLR, German Aerospace Research Establishment. The authors thank Philippe Scouflaire for his technical support and Lucien Vingert, Alain Mouthon, and Roger Barraud for their help with the experiments.

References

[1] Herding, G., Snyder, R., Scouflaire, P., Rolon, C., and Candel, S., "Flame Stabilization in Cryogenic Propellant Combustion," *26th Symposium (International) on Combustion*, The Combustion Inst., Pittsburgh, PA, 1996, pp. 2041–2047.

[2] Mayer, W., and Tamura, H., "Propellant Injection in a Liquid Oxygen/Gaseous Hydrogen Rocket Engine," *Journal of Propulsion and Power*, Vol. 12, No. 6, 1996, pp. 1137–1147.

[3] Beyler, C. L., and Gouldin, F. C., "Flame Structure in a Swirl Stabilized Combustor Inferred by Radiant Emission Measurements," *18th Symposium (International) on Combustion*, The Combustion Inst., Pittsburgh, PA, 1981, pp. 1011–1019.

[4] Vogel, A., "Investigations on Atomization of a Coaxial H_2/LOX Jet Under Hot Fire Conditions," *Proceedings of the 6th International Conference on Liquid Atomization and Spray Systems*, edited by A. J. Yule and C. Dumouchel, Begell House, New York, 1994.

[5] Snyder, R., Herding, G., Rolon, C., and Candel, S., "Analysis of Flame Patterns in Cryogenic Propellant Combustion," *Combustion Science and Technology*, Vol. 124, No. 1–6, 1997, pp. 331–370.

[6] Tatum, J., and Jarowski, W., "A Solution of Abel's Equation," *Journal of Quantitative Spectroscopy and Radiative Transfer*, Vol. 38, 1987, pp. 319–322.

[7] Hughey, B. J., and Santavicca, D. A., "A Comparison of Techniques for Reconstructing Axisymmetric Reacting Flow Fields from Absorption Measurements," *Combustion Science and Technology*, Vol. 29, 1982, pp. 167–190.

[8] Ravichandran, M., and Gouldin, F. C., "Determination of Temperature and Concentration Profiles Using (a Limited Number of) Absorption Measurements," *Combustion Science and Technology*, Vol. 45, 1986, pp. 47–64.

[9] Brummund, U., Cessou, A., Oschwald, M., Vogel, A., Grisch, F., Bouchardy, P., Pealat, M., Vingert, L., Habiballah, M., Snyder, R., Herding, G., Scouflaire, P., Rolon, C., and Candel, S., "Laser Diagnostics for Cryogenic Propellant Combustion Studies," *Proceedings of the 2nd International Symposium on Liquid Rocket Propulsion* (Chatillon, France), 1995, pp. 19.1–19.22.

[10] Hopfinger, E., and Lasheras, J. C., "Breakup of a Water Jet in High Velocity Co-Flowing Air," *Proceedings of the 6th International Conference on Liquid Atomization*, edited by A. J. Yule and C. Dumouchel, Begell House, New York, 1994, pp. 110–117.

Color reproductions courtesy of the Centre National de la Recherche Scientifique.